ADVANCED MATERIALS
www.advmat.de

Atomic-Scale Tracking Topological Phase Transition Dynamics of Polar Vortex-Antivortex Pairs

Ruixue Zhu, Sizheng Zheng, Xiaomei Li, Tao Wang, Congbing Tan, Tiancheng Yu, Zhetong Liu, Xinqiang Wang, Jiangyu Li,* Jie Wang,* and Peng Gao**

Non-trivial topological structures, such as vortex-antivortex (V-AV) pairs, have garnered significant attention in the field of condensed matter physics. However, the detailed topological phase transition dynamics of V-AV pairs, encompassing behaviors like self-annihilation, motion, and dissociation, have remained elusive in real space. Here, polar V-AV pairs are employed as a model system, and their transition pathways are tracked with atomic-scale resolution, facilitated by in situ (scanning) transmission electron microscopy and phase field simulations. This investigation reveals that polar vortices and antivortices can stably coexist as bound pairs at room temperature, and their polarization decreases with heating. No dissociation behavior is observed between the V-AV phase at room temperature and the paraelectric phase at high temperature. However, the application of electric fields can promote the approach of vortex and antivortex cores, ultimately leading to their annihilation near the interface. Revealing the transition process mediated by polar V-AV pairs at the atomic scale, particularly the role of polar antivortex, provides new insights into understanding the topological phases of matter and their topological phase transitions. Moreover, the detailed exploration of the dynamics of polar V-AV pairs under thermal and electrical fields lays a solid foundation for their potential applications in electronic devices.

1. Introduction

Topological structures and their mediated topological phase transitions have attracted considerable attention, due to their fundamental scientific significance and their potential practical applications in electronic devices.[1] Of particular interest are vortex-antivortex (V-AV) pairs, which play a critical role in understanding superconductors,[2,3] superfluids,[4] and various other exotic properties.[5–7] V-AV pairs are expected to exhibit diverse dynamic behaviors, such as motion and self-annihilation, as supported by sufficient theoretical investigations.[8,9] In addition, the emergence and dissociation of quasi-long-range ordered V-AV pairs driven by thermal fields has also been confirmed in 2D spin systems,[10] a phenomenon known within the framework of the Berezinskii–Kosterlitz–Thouless (BKT) phase transition theory.[11–15]

Limited by existing characterization techniques, obtaining reliable experimental evidence regarding the detailed evolutions of V-AV pairs in real space remains a challenge. For example, the commonly used Lorentz transmission electron microscopy (LTEM) for studying magnetic topologies suffers from vulnerable phase contrast, making the LTEM results highly sensitive to experimental conditions such as defocus.[16–19] Moreover, due to the weak magnetic signal in quasi-2D magnetic materials, LTEM usually requires a large defocus to record

R. Zhu, X. Li, T. Wang, T. Yu, Z. Liu, P. Gao
Electron Microscopy Laboratory
and International Center for Quantum Materials
School of Physics
Peking University
Beijing 100871, China
E-mail: pgao@pku.edu.cn

S. Zheng, J. Wang
Department of Engineering Mechanics
Zhejiang University
Hangzhou, Zhejiang 310027, China
E-mail: jw@zju.edu.cn

X. Li
School of Integrated Circuits
East China Normal University
Shanghai 200241, China

The ORCID identification number(s) for the author(s) of this article can be found under https://doi.org/10.1002/adma.202312072

DOI: 10.1002/adma.202312072

C. Tan
Hunan Provincial Key Laboratory of Intelligent Sensors and Advanced Sensor Materials
School of Physics and Electronics
Hunan University of Science and Technology
Xiangtan, Hunan 411201, China
E-mail: cbtan@xtu.edu.cn

X. Wang
State Key Laboratory of Artificial Microstructure and Mesoscopic Physics
School of Physics
Peking University
Beijing 100871, China

X. Wang, P. Gao
Collaborative Innovation Centre of Quantum Matter
Beijing 100871, China

J. Li
Guangdong Provincial Key Laboratory of Functional Oxide Materials and Devices
Southern University of Science and Technology
Shenzhen, Guangdong 518055, China
E-mail: lijy@sustech.edu.cn

data,[20] thereby preventing the realization of ultrahigh spatial resolution. Expanding the scope of research to the field of ferroelectrics, several simulation studies have predicted the occurrence of a BKT phase transition in 2D electric dipole systems with an increase in temperature, accompanied by a power-law decay of the correlation function.[21–23] However, conclusive experimental evidence is still lacking. A few studies have aimed to reveal the evolutions of polar V-AV pairs. Using atomic force microscopy, Chae et al. find that the temperature-dependence transition of pairwise polar vortices in layered hexagonal $ErMnO_3$ is not of the BKT type.[24] Additionally, Kim et al. demonstrated the biased-tip-induced creation and separation of a polar V-AV pair in $BiFeO_3$ film using angle-resolved lateral piezoresponse force microscopy (PFM) at the hundred-nanometer scale.[25] The PFM contrast is generally sensitive to multiple external factors, such as the coupling of the tip and moving cantilever, and it is difficult to distinguish the contribution of ion potential and polarization charge, making data interpretation vulnerable.[26–29] When considering spatial resolution, the characterization techniques available for ferroelectrics are superior to those for ferromagnets. Various atomic imaging techniques based on a transmission electron microscope (TEM) can precisely map subunit-scale polar dipoles,[30–33] enabling in situ tracking of the topological phase transition dynamics of polar V-AV pairs even more compelling.

The $PbTiO_3$(PTO)/$SrTiO_3$(STO) superlattice serves as a paradigmatic framework for the investigation of various polar topologies, involving flux-closures,[34–36] vortices,[37,38] and skyrmion bubbles,[39] along with their topological phase transitions in response to external stimuli.[40–48] Previous simulations based on first principles calculations have predicted the formation of polar V-AV pairs consisting of electric dipoles in $(PTO)_n/(STO)_n$ ($n = 3, 6$) superlattices.[49] Furthermore, through carefully manipulating the layer thickness of PTO/STO superlattices grown on $DyScO_3$ (DSO) substrates, Adeel et al. have successfully demonstrated the stable existence of polar V-AV pairs at room temperature in experiments, thanks to the delicate tuning of elastic, electrostatic and gradient energies.[50–53] In contrast to the alternating clockwise and counterclockwise vortex arrays that are located within the PTO layers with their formation primarily dependent on elastic conditions, the antivortex arrays are observed within the confined paraelectric STO layers, displaying a strong dependence on electric fields and a relatively weaker sensitivity to strain.

In this context, we consider polar V-AV pairs in the fabricated quasi-2D $(PTO)_{11}/(STO)_6$ superlattice lamella as the ground state to investigate their possible dynamic behaviors under thermal and electrical stimuli in real space. As schematically shown in **Figure 1a**, the terminals of thermal- and electric-field-induced transition are disordered paraelectric phase and long-range-ordered ferroelectric monodomain. Combining atomically resolved in situ spherical aberration-corrected transmission electron microscopy and phase-field simulation, we find that polar vortex and antivortex coexist and behave as bound pairs over a wide temperature range, but their polarization magnitude gradually decreases upon heating. No unbinding of polar V-AV pairs occurs between the ground state and the paraelectric state. In addition, an electric field can promote the motion and approach of adjacent vortex cores and antivortex cores, culminating in their annihilation near the interface. Our findings reveal the dynamic details of polar V-AV pairs at the scale of an electric dipole and provide useful information for their potential applications in the future, as well as effective guidance for exploring the associated BKT phase transition in ferroelectric materials.

2. Results and Discussion

Guided by the phase diagram of polar V-AV pair dependent on the PTO/STO layer thickness,[50] we grew $(PTO)_{11}/(STO)_6$ superlattices on DSO substrates using pulsed laser deposition for this study, with embedded $SrRuO_3$ (SRO) layer serving as the bottom electrode (details in the Experimental Section, Supporting Information). A typical atomic-scale middle angle annular dark field (MAADF) scanning transmission electron microscopy (STEM) image taken along the (010) zone axis reveals alternate PTO and STO layers with sharp and coherent interfaces (Figure 1b). Vortex arrays exist in the PTO layers, as evident from the alternating high and low diffraction contrast in the TEM dark-field image (Figure 1c) and the weak strain contrast observed in the MAADF image. A magnified high-angle annular dark field (HAADF) image is shown in Figure 1d, from which we can derive the displacement of Ti relative to the four neighboring cations and subsequently calculate the polarization (details in the Experimental Section, Supporting Information).[30] The local polar vector map is plotted in the left panel of Figure 1e, confirming the existence of bound V-AV pairs within the superlattice (complete maps of polarization orientation and magnitude are shown in Figures S1 and S2, Supporting Information). Notably, antivortices in the STO layer are sandwiched between pairs of aligned vortices with the same circulation in adjacent PTO layers, in good agreement with the phase field simulation results depicted in the middle and right panels.

The distribution of polar V-AV pairs can be reflected by the unit-cell-level maps of out-of-plane lattice constant **c** (Figure 1f) and in-plane lattice constant *a* (Figure 1g). These maps were calculated based on Figure 1d and showed strong consistency with the simulation results in Figure 1h,i. Obviously, the *c*-color map in Figure 1f exhibits a characteristic orange sinusoidal wave pattern within the PTO layers, with local maxima corresponding to the most strained vortex cores, marked by purple balls. Notably, the staggered vortex cores are located at different heights. In addition, the *a*-color map in Figure 1g also helps identify the vortex cores, which are located at the vertices of the orange triangles. In the STO layer, the inhomogeneous *a*-color map exhibits an orange-colored wave feature, which is more pronounced in the simulation image (Figure 1i). The antivortex cores are located in the gaps of the orange wave, denoted by orange balls. Apart from lattice analysis, we also carried out accurate quantitative measurements of the out-of-plane polarization $\mathbf{p}_z$ and in-plane polarization $\mathbf{p}_x$ of Ti cations. Corresponding color-magnitude maps are

J. Li
Department of Materials Science and Engineering
Southern University of Science and Technology
Shenzhen, Guangdong 518055, China
J. Wang
Zhejiang Laboratory
Hangzhou 311100, China

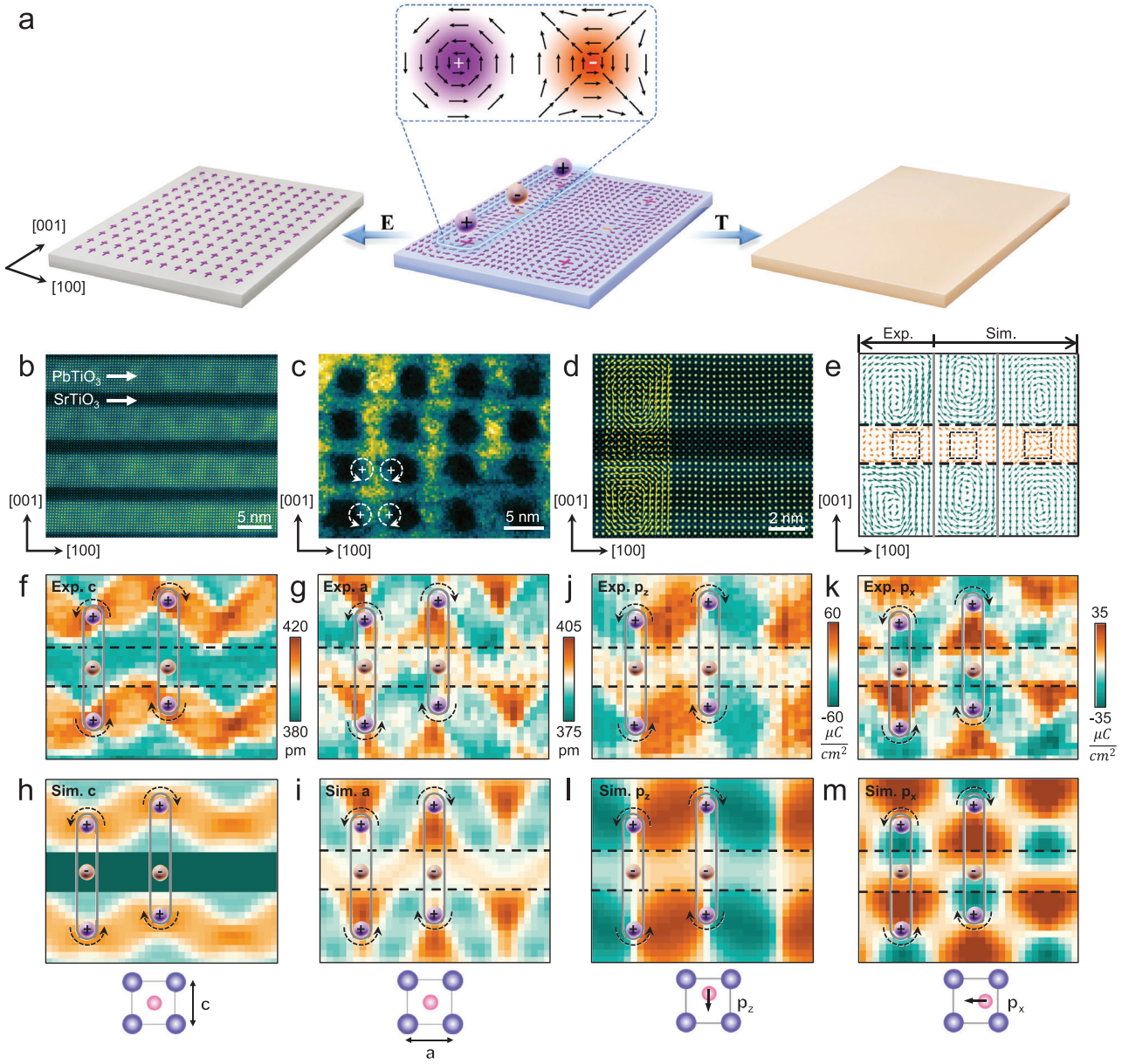

Figure 1. Characterization and quantitative analysis of polar V-AV pairs in designed $(PTO)_{11}/(STO)_6$ superlattice. a) Evolution diagram of polar V-AV pairs under thermal (T) and electric (E) fields. The purple balls represent vortices with the topological number of +1, and the orange balls represent antivortices with the topological number of −1. b,c) Low-magnification MAADF-STEM image (b) and TEM dark-field image (c) formed by reflection with $g = 002$, showing the high quality of the designed $(PTO)_{11}/(STO)_6$ superlattice and the diffraction contrast of polar vortex arrays in PTO layers. d) An enlarged atomically resolved HAADF-STEM image of a 6-u.c. thick STO layer sandwiched between two 11-u.c. thick PTO layers. The HAADF image is partially overlaid with yellow arrows, denoting polar vectors calculated from the off-center displacement of Ti. The polar vector map derived from (d) and the simulation results are depicted together in (e), demonstrating high consistency. The arrows on the rightmost panel in (e) are unified to the same length to highlight the antivortex configuration. f,g) The unit-cell-scale mappings of lattice **c** (f) and lattice **a** (g) extracted from (d). h,i) Corresponding simulation results of lattice **c** (h) and lattice **a** (i). j,k) The unit-cell-scale mappings of out-of-plane polarization $\mathbf{p_z}$ (j) and in-plane polarization $\mathbf{p_x}$ (k). l,m) Corresponding simulation results of $\mathbf{p_z}$ (l) and $\mathbf{p_x}$ (m). The black rotation arrows indicate the rotation direction of polar vortices. Insets: calculation sketches of **c**, **a**, $\mathbf{p_z}$, and $\mathbf{p_x}$.

displayed in Figure 1j,k, showing good agreement with the simulation results in Figure 1l,m. In reference to the polar vector map in Figure 1e, it is evident that the polarization distribution of the vortex is asymmetric, manifested by unequal in-plane domains and zig-zag vortex cores.[33]

Taking polar V-AV pairs as the ground state, we delved deeper into their thermally responsive behaviors through in situ heating experiments. As schematically shown in Figure S3 (Supporting Information), we first used the focused ion beam (FIB) method to cut and acquire quasi-2D lamellas from the epitaxially grown

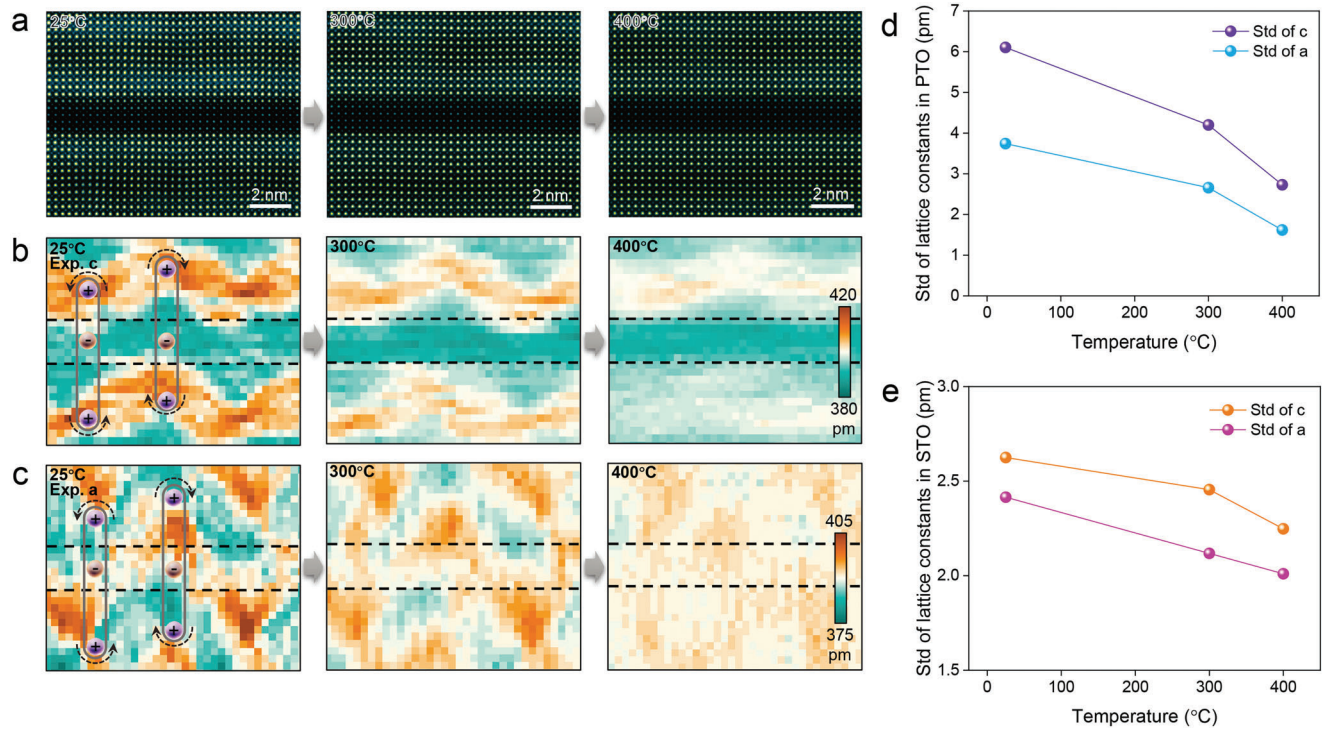

Figure 2. Real-space evolution of polar V-AV pairs under thermal excitation at the atomic scale. a) A series of HAADF-STEM images acquired with increasing temperature. b,c) The corresponding unit-cell-scale mapping series of out-of-plane lattice **c** (b) and in-plane lattice **a** (c) are derived from (a), indicating the disappearance of polar V-AV pairs. d,e) Std of lattice **c** and lattice **a** in PTO layers (d) and STO layers (e) as a function of temperature, with decreasing trends representing the lattice constant distribution from discrete to uniform.

superlattice film. Subsequently, we transferred these lamellas to specially designed E-chips to conduct in situ experiments (further experimental details can be found in the Experimental Section, Supporting Information). During the heating process, we collected atomically resolved HAADF images at different temperatures, including 25, 300, and 400 °C, as shown in **Figure 2a** (Temperature–Time curve is plotted in Figure S4, Supporting Information). Following image acquisition, Gaussian fitting was employed to accurately determine the positions of atomic columns, enabling quantitative analysis. The initial color maps of lattice constants, featured in Figure 2b,c, portrayed characteristic sinusoidal waves associated with polar V-AV pairs. With the temperature increases, the orange sinusoidal patterns in the PTO layers become less pronounced (Figure 2b), indicating a reduction and homogenization of the out-of-plane strain. This corresponds to the disappearance of polar vortices, aligning with our simulations (Figure S5, Supporting Information). Focusing on the *a*-color map change in the STO layer (see Figure 2c), the previously inhomogeneous in-plane strain transformed into a uniform distribution, reflecting the thermal erasure of antivortices. Notably, the change in lattice constants caused by thermal expansion below 400 °C has been evaluated to be less than 2 pm and can be ignored (see details in Supporting Information Text).[54,55] On this basis, we performed further quantitative statistics of the lattice constants *c* and *a*, using the standard deviation (std) as a metric (Figure 2d,e; Figure S6, Supporting Information). We calculate the std using the formula $\mathrm{Std}_{T\,^\circ\mathrm{C}} = \sqrt{\frac{1}{n}\sum\left(x_{T\,^\circ\mathrm{C}} - \bar{x}_{T\,^\circ\mathrm{C}}\right)^2}$, where $x_{T°C}$ represents each lattice constant value at T °C, $\bar{x}_{T\,^\circ\mathrm{C}}$ denotes the mean value at T °C, and n indicates the total number of data points. With heating, the stds of both lattice *c* and lattice *a* in PTO and STO layers displayed a decreasing trend, signifying a reduction in the dispersion of lattice constants attributed to the disappearance of polar structures. For comparative purposes, we also conducted a similar quantitative analysis on a $(PTO)_7/(STO)_{13}$ superlattice that exclusively contains vortex, lacking antivortex (Figure S7, Supporting Information). Indeed, the stds of *c* and *a* in the STO layer devoid of antivortex was relatively lower than those in the $(PTO)_{11}/(STO)_6$ superlattice, which contains antivortex.

The thermal evolution of polar V-AV pairs is further illuminated through unit-cell-scale measurements of out-of-plane polarization $\mathbf{p}_z$ and in-plane polarization $\mathbf{p}_x$, as shown in **Figure 3a,b**. The profiles depicting variations of polarization magnitude, corresponding to the black dashed frames, provide quantitative insights into the reduction in ferroelectricity with increasing temperature, as depicted in Figure 3c,d. The topological phase transition from V-AV pairs to the paraelectric phase occurs at ≈400 °C. It is worth noting that vortex and antivortex consistently coexist as bound pairs, without any annihilation or separation into isolated individuals. Nevertheless, at T = 370 °C, the average polarization of the antivortex measures only ≈0.43 μC cm^{-2}, signifying the near disappearance of its ferroelectric character. At this time, the average polarization of the vortex remains relatively high, ≈4.06 μC cm^{-2}. This suggests that the polar antivortex may disappear prior to the polar vortex during

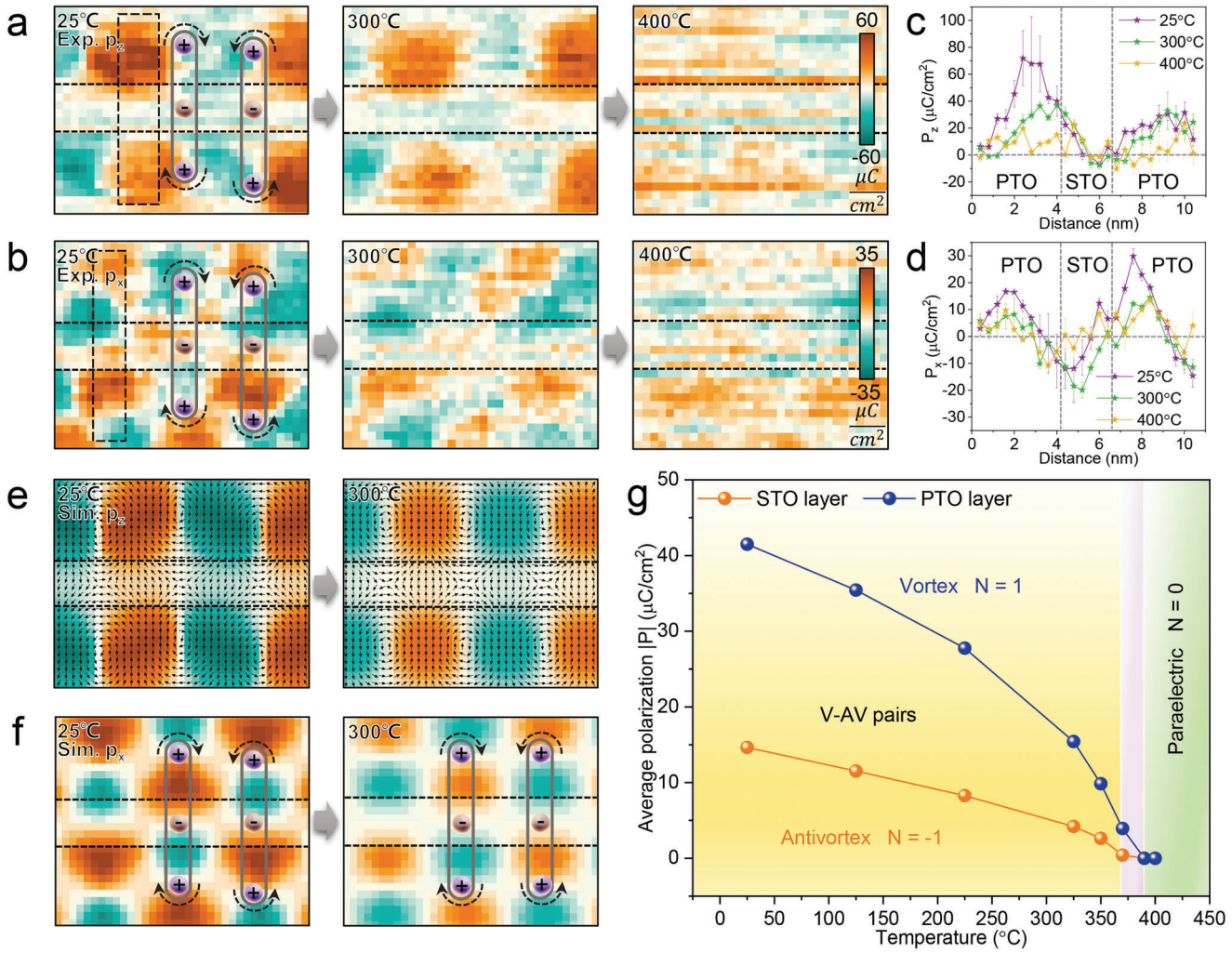

Figure 3. Thermal field induced variation of polarization at the atomic scale. a,b) Out-of-plane polarization $\mathbf{p_z}$ (a) and in-plane polarization $\mathbf{p_x}$ (b) mapping series derived from the atomically resolved HAADF-STEM images acquired during heating. The critical Curie temperature is ≈400 °C. c,d) Vertical $\mathbf{p_z}$ (c) and $\mathbf{p_x}$ (d) line profiles corresponding to the black dashed frames in (a,b), respectively. The magnitude of $\mathbf{p_z}$ and $\mathbf{p_x}$ decrease during heating, culminating with the formation of the paraelectric phase. e,f) Simulation results corresponding to the variation of $\mathbf{p_z}$ (e) and $\mathbf{p_x}$ (f). g) Temperature phase diagram of polar V-AV pairs, showing the temperature dependence of the average polarization |P|. N represents the topological number.

the heating process, primarily due to the dependence of antivortex stability on bound charges provided by adjacent vortices.[50] Moreover, our simulations reveal that the staggered vortex cores, present at room temperature, tend to align horizontally at high temperatures, as evident from Figure 3e,f. This realignment is attributed to the combined effects of increased Landau energy and decreased elastic energy, as detailed in Figure S8 (Supporting Information).[56] In accordance with the phase field simulations, we have constructed a temperature phase diagram, as shown in Figure 3g, elucidating the temperature-dependent variations in the average polarization, denoted as |P|. This diagram is divided into three regions: i) 25–370 °C, where V-AV pairs are dominant; ii) 370–400 °C, during which antivortex disappears while vortex persists; iii) temperatures exceeding 400 °C, leading to the formation of a disordered paraelectric phase.

Connecting the bottom electrode SRO and the carbon layer deposited on the film surface to the positive and negative electrodes respectively enables the application of electric fields to the polar V-AV pairs to further explore their electrical response behaviors. A series of typical dark-field TEM images (**Figure** 4a) depicts alternating bright and dark dotted-like regions initially representing vortex arrays, which then evolve into tilted stripes, indicating a topological phase transition from the vortex phase to trivial a/c domains (Figure S9, Supporting Information).[42,45] Geometric phase analysis of low-magnification atomic images revealed similar results (Figure S10, Supporting Information). With a further increase in the applied electric field, the PTO layers manifest a uniformly polarized state, indicative of the formation of ferroelectric monodomains. Simulation results mirror this transition process consistently (Figure 4b; Figure S11, Supporting Information). Note that upon removal of the electric field, the vortex state can be restored (Figure S12, Movie S1, Supporting Information). An intriguing finding is that the cores of the vortex and antivortex respond to the electric field by moving and approaching each

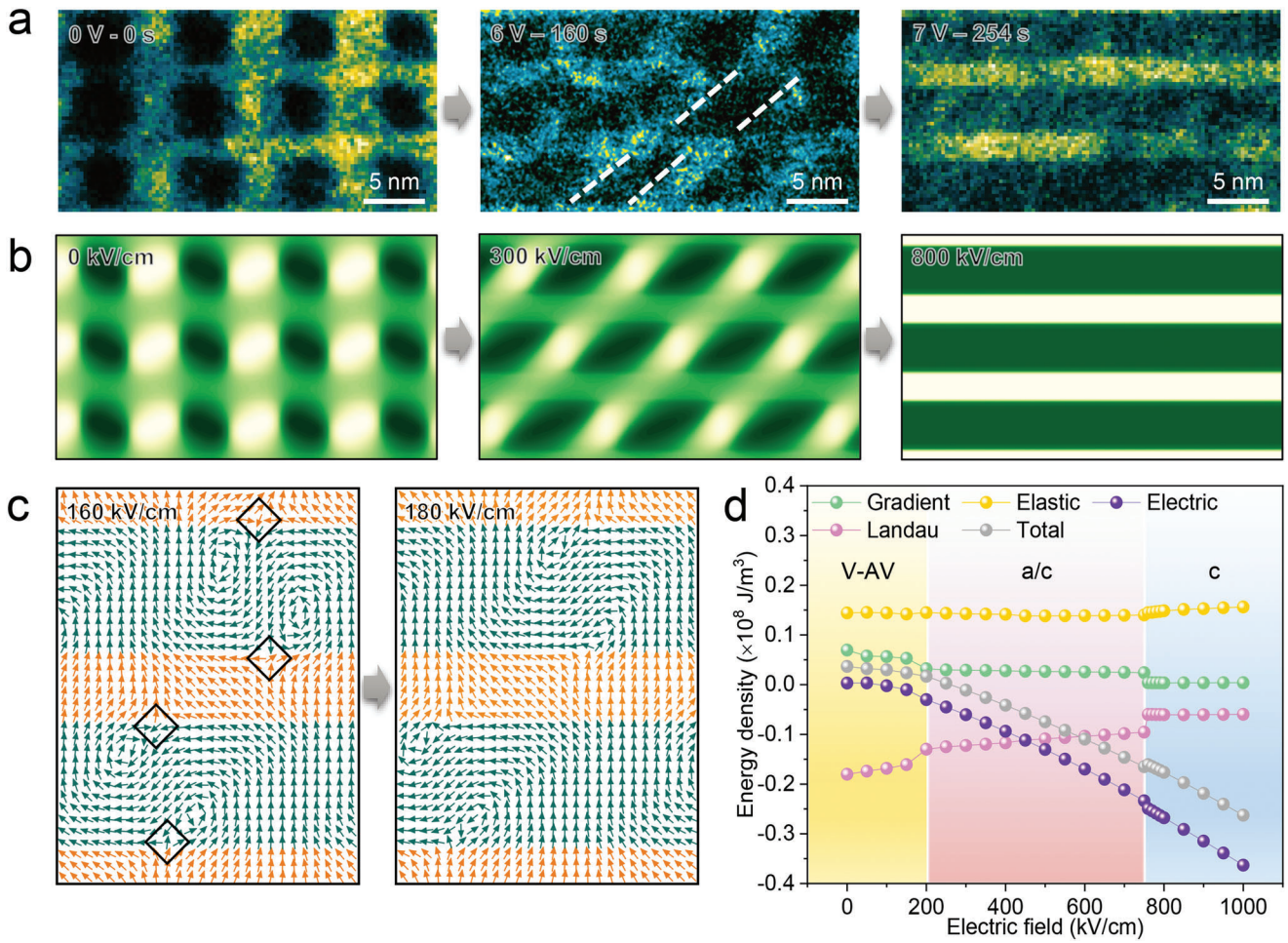

Figure 4. Real-space evolution of polar V-AV pairs under electric excitation. a) Low magnification TEM dark-field image series formed by reflection with $g = 002$, displaying the transformation from V-AV pairs to monodomain under applied electric bias, with a/c domain intermediate phase as outlined by the white dashed lines. b) The corresponding phase field simulation results in the spatial distribution of out-of-plane polarization under electric fields. c) Simulated polar maps of intermediate states captured at ≈160 and ≈180 kV cm^{-1}. The black frames highlight the antivortex cores. d) Electric field phase diagram of polar V-AV pairs, showing the evolution of energy components. Three regions can be found in which V-AV pairs, a/c domains, and c domains are dominant, respectively.

other until their ultimate annihilation near the interface. The corresponding dipole evolution is visually depicted in Figure 4c. Furthermore, a phase diagram has been conducted to illustrate the electric-field-dependent evolution of polar V-AV pairs along with their energy changes (Figure 4d). Three regions are divided: i) 0–200 kV cm^{-1}, V-AV pairs are dominant; ii) 200–750 kV cm^{-1}, V-AV pairs are broken and a/c domains are dominant; iii) above 750 kV cm^{-1}, with c domains emerging as the dominant phase.

The underlying mechanisms of these phenomena are discussed briefly below. In magnetic systems, the interaction between vortex and antivortex, composed of spins, is generally attractive, leading to their self-annihilation when they come into close proximity.[9,57] Stable-bound V-AV pairs are only possible under specific scenarios, such as when they are confined within narrow temperature ranges or subject to particular pining states.[58–61] The dissociation of V-AV pairs occurs at the BKT transition temperature, resulting in the appearance of isolated free vortices.[2,62] In contrast, within our ferroelectric superlattice regime, polar V-AV pairs can spontaneously form under delicate strain and electrostatic boundary conditions. They remain stable at room temperature in the absence of external fields. The pinning effect of the interface prevents their self-annihilation, but the application of an electric field can promote the approach of vortex and antivortex cores to each other, leading to their annihilation near the interface. Furthermore, during heating, no binding-unbinding phenomenon of polar V-AV pairs is observed. One possible explanation for this observation could be the presence of the PTO/STO interface, which introduces a pinning potential that significantly perturbs the separation of polar V-AV pairs. It's crucial to emphasize that the topological phase transition dynamics of the polar antivortex in STO layers are closely related to those of the polar vortex in PTO layers since the stability of the polar antivortex depends on the electrostatic conditions established by the adjacent polar vortex.

In addition, in our study, we prepared nanometer-thick lamellas from the PTO/STO superlattice films through FIB etching, introducing a change in strain conditions compared to the

as-obtained thin film. The original biaxial strain provided by the substrate transforms into a uniaxial strain,[63] which may lead to polar structure reconstruction and phase transition pathways that differ from those studied using X-ray diffraction techniques.[43,44] Particularly, in our case, the high-temperature a_1/a_2 phase was not observed.

3. Conclusion

We have employed room-temperature polar V-AV pairs as the ground state to quantitatively investigate their topological phase transition dynamics under thermal and electric fields, achieving atomic-level spatial resolution. During the heating process, the polarization magnitude gradually decreases. The polar antivortex disappeared prior to the polar vortex, and no dissociation-like behavior of polar V-AV pairs was observed. The superlattice interface facilitates the formation of polar V-AV pairs, while on the other hand seems to prevent their dissociation and self-annihilation. However, under the action of electric fields, the cores of adjacent polar vortex and antivortex gradually approach each other and annihilate near the interface, resulting in the transition from the vortex phase to a/c domains. Our in situ investigation of polar V-AV pairs in PTO/STO superlattice lamella sheds light on their role in mediating topological phase transitions under thermal and electric fields, laying the groundwork for future experimental exploration of ferroelectric BKT phase transitions. Furthermore, the dynamic details revealed at the atomic scale provide essential information for the design of devices based on them.

4. Experimental Section

Fabrication of Superlattice: The SRO bottom electrodes were epitaxial grown on (110)-DSO substrates by pulsed laser deposition (PVD-5000, with a 248 nm KrF excimer laser). The PTO_{11}/STO_6 superlattices were then deposited using the deposition parameters given in the previous literature.[63] The PTO ferroelectric layer was deposited from a 2-inch target with 10% excess Pb ($Pb_{1.1}TiO_3$) to compensate for Pb volatility. A nominally stoichiometric STO target was used to deposit dielectric layer STO. Alternative PTO and STO layers were deposited with the substrate held at a temperature of 600 °C and oxygen pressure of 200 mTorr. Laser energy fine-tuning for the growth of the SRO, PTO, and STO sublayers was crucial for the presence of a polar vortex-antivortex pair in the superlattice. The sublayers' thicknesses were held by controlling the laser pulse number. After deposition, the superlattice films were cooled to room temperature at 20 °C min^{-1} under a 200-mTorr oxygen pressure.

TEM Sample Preparation: Cross-sectional TEM samples for in situ thermal and electrical experiments were prepared using focused ion beam (Helios G4) etching. As illustrated in Figure S3 (Supporting Information), nanometer-thick lamellas were obtained from the epitaxially grown PTO/STO superlattice film through ion beam processing and were then transferred to custom-made chips provided by Protochips, Inc. The TEM sample for heating was positioned on the integrated hole of the chip, whereas the sample for applying external bias was fixed on two Pt electrodes.

Electron Microscopy Characterization and Quantitative Analysis: In situ (S)TEM experiments were performed with a Protochips double-tilt holder, and the process was observed using an aberration-corrected FEI Titan Themis G2 at an accelerating voltage of 300 kV. Dark field TEM images were acquired under the two-beam condition with $g = 002$. The convergence semi-angle for STEM imaging was 30 mrad, and the collection semi-angle snap was 50 to 200 mrad for HAADF and 39 to 200 mrad for MAADF. The atom positions were determined by simultaneously fitting 2D Gaussian peaks using homemade MATLAB codes. For ABO_3-type perovskite oxide, the geometric center of the four heavier A-site atoms was considered as the centrosymmetric position, denoted by coordinates (x_1, y_1), while the coordinates of the B-site atom were represented by (x_2, y_2). The off-center displacement (δ) between the B-site atom and the selected geometric center could be readily calculated as $\delta = \sqrt{(x_2 - x_1)^2 + (y_2 - y_1)^2}$. The relationship between polarization and displacement was expressed by the following formula:[64] $P_s = \frac{1}{\nu}\sum_i \delta_i Z_i$, where ν is the volume of the unit cell, δ represents the displacement between the atoms and the selected geometric center, and Z is the Born effective charge of atoms, defining the polarization change per unit displacement. In this system, $Z = 6.71$ for Ti in PTO and $Z = 7.12$ for Ti in STO.[65]

Phase Field Simulation: In order to accurately predict the topological phase transition of vortex-antivortex pairs in superlattices, a phase field model with polarization-dependent elastic and electrostrictive coefficients was adopted.[66] The free energy density in the phase field model was as follows

$$\begin{aligned} f\left[\left\{\varepsilon_{ij}\right\}, \{E_i\}, \{P_i\}, \left\{P_{i,j}\right\}\right] &= \alpha_{ij}P_iP_j + \alpha_{ijkl}P_iP_jP_kP_l + \alpha_{ijklmn}P_iP_jP_kP_lP_mP_n + \frac{1}{2}g_{ijkl}P_{i,j}P_{k,l} \\ &+ \frac{1}{2}\left(c_{ijkl} + a_{ijklmn}P_mP_n\right)\varepsilon_{ij}\varepsilon_{kl} - \left(q_{ijkl} + b_{ijklmn}P_mP_n\right)\varepsilon_{ij}P_kP_l \\ &- \frac{1}{2}\kappa_0\kappa_{ij}E_iE_j - E_iP_i \end{aligned} \quad (1)$$

in which P_i, ε_{ij} and E_i are the spontaneous polarization, strain, and electric field components, respectively. α_{ij}, α_{ijkl} and α_{ijklmn} are the Landau energy coefficients, g_{ijkl} are the gradient energy coefficients, κ_0 is the vacuum permittivity and κ_{ij} are the background dielectric constants. c_{ijkl} and q_{ijkl} are elastic and electrostrictive coefficients of the paraelectric state, respectively. In order to accurately model the elasticity and electromechanical coupling properties of the ferroelectric phase, the polarization-dependent elastic coefficients $a_{ijklmn}P_mP_n$ and electrostrictive coefficients $b_{ijklmn}P_mP_n$ were added to the coefficients of elastic and electrostrictive energy densities, respectively, in Equation (1). In which a_{ijklmn} were obtained by fitting the results of experimental measurement,[67] whereas b_{ijklmn} were derived by using a similar approach to that of q_{ijkl}.[68] The polarization-dependent elastic and electrostrictive coefficients had the advantage to adjust the properties of elasticity and electromechanical coupling in the ferroelectric phase automatically with the change in polarization. These polarization-dependent coefficients would reduce to zero when the polarization disappears in the paraelectric phase, see Table S1 and text (Supporting Information) for details. All repeating subscripts in Equation (1) imply summation over the Cartesian coordinate components x_i ($i = 1, 2,$ and 3), and "$,i$" denotes the partial derivative operator with respect to x_i ($\partial/\partial x_i$).

The temporal evolution of the polarization could be described by the time-dependent Ginzburg–Landau (TDGL) equations as $\frac{\partial P_i(\boldsymbol{r},t)}{\partial t} = -L\frac{\delta F}{\delta P_i(\boldsymbol{r},t)}$, where L represents the domain wall mobility, $F = \int_V f\, dV$ is the total free energy in the whole simulated system, $\boldsymbol{r}$ and t denote the spatial position vector and time, respectively. In addition, both the mechanical equilibrium equations $\sigma_{ij,j} = \frac{\partial}{\partial x_j}\left(\frac{\partial f}{\partial \varepsilon_{ij}}\right) = 0$ and the Maxwell's equation $D_{i,i} = -\frac{\partial}{\partial x_i}\left(\frac{\partial f}{\partial E_i}\right) = 0$ were satisfied simultaneously for a body-force-free and charge-free ferroelectric system, where σ_{ij} and D_i are the stress and electric displacement components, respectively.

Supporting Information

Supporting Information is available from the Wiley Online Library or from the author.

Acknowledgements

R.X.Z., S.Z.Z., X.M.L., and T.W. contributed equally to this work. This work was supported by the Guangdong Basic and Applied Basic Research

Foundation (2023B1515130003), the open research fund of Songshan Lake Materials Laboratory (2022SLABFK03), Key-Area Research and Development Program of Guangdong Province (2018B030327001, 2020B010189001), the Guangdong Provincial Key Laboratory Program (2021B1212040001) from the Department of Science and Technology of Guangdong Province, National Program on Key Basic Research Project (2022YFB3807601). The sample growth was supported by the open research fund of Songshan Lake Materials Laboratory (2021SLABFN14), the Hunan Provincial Natural Science Foundation of China (2021JJ30234), the Scientific Research Fund of Hunan Provincial Education Department (21A0311). P.G. acknowledges the support from the New Cornerstone Science Foundation through the XPLORER PRIZE. The authors also thank the Electron Microscopy Laboratory at Peking University for the use of the Cs-corrected electron microscope.

Conflict of Interest

The authors declare no conflict of interest.

Data Availability Statement

The data that support the findings of this study are available from the corresponding author upon reasonable request.

Keywords

ferroelectrics, in situ (scanning) transmission electron microscopy, polar topological structures, polar vortex-antivortex pairs, topological phase transitions

Received: November 13, 2023
Revised: April 2, 2024
Published online:

[1] J. M. Kosterlitz, D. J. Thouless, *J. Phys. C: Solid State Phys.* **1973**, *6*, 1181.
[2] M. Beasley, J. Mooij, T. Orlando, *Phys. Rev. Lett.* **1979**, *42*, 1165.
[3] A. Hebard, A. Fiory, *Phys. Rev. Lett.* **1980**, *44*, 291.
[4] D. Bishop, J. Reppy, *Phys. Rev. Lett.* **1978**, *40*, 1727.
[5] D. Resnick, J. Garland, J. Boyd, S. Shoemaker, R. Newrock, *Phys. Rev. Lett.* **1981**, *47*, 1542.
[6] J. Fröhlich, T. Spencer, *Commun. Math. Phys.* **1981**, *81*, 527.
[7] A. K. Yadav, K. X. Nguyen, Z. Hong, P. García-Fernández, P. Aguado-Puente, C. T. Nelson, S. Das, B. Prasad, D. Kwon, S. Cheema, *Nature* **2019**, *565*, 468.
[8] G. Roumpos, M. D. Fraser, A. Löffler, S. Höfling, A. Forchel, Y. Yamamoto, *Nat. Phys.* **2011**, *7*, 129.
[9] A. Chaves, F. Peeters, G. Farias, M. Milošević, *Phys. Rev. B* **2011**, *83*, 054516.
[10] M. J. Beach, A. Golubeva, R. G. Melko, *Phys. Rev. B* **2018**, *97*, 045207.
[11] N. D. Mermin, H. Wagner, *Phys. Rev. Lett.* **1966**, *17*, 1133.
[12] V. Berezinskii, *J. Exp. Theor. Phys.* **1972**, *34*, 610.
[13] J. Kosterlitz, *J. Phys. C: Solid State Phys.* **1974**, *7*, 1046.
[14] P. Meisenheimer, H. Zhang, D. Raftrey, X. Chen, Y.-T. Shao, Y.-T. Chan, R. Yalisove, R. Chen, J. Yao, M. C. Scott, *Nat. Commun.* **2023**, *14*, 3744.
[15] T. Domröse, T. Danz, S. F. Schaible, K. Rossnagel, S. V. Yalunin, C. Ropers, *Nat. Mater.* **2023**, *22*, 1345.
[16] Y. Togawa, T. Akashi, H. Kasai, G. W. Paterson, S. McVitie, Y. Kousaka, H. Shinada, J. Kishine, J. Akimitsu, *J. Phys. Soc. Jpn.* **2021**, *90*, 014702.
[17] X. Yu, *JPSJ News Comments* **2021**, *18*, 01.
[18] Y. Yao, B. Ding, J. Liang, H. Li, X. Shen, R. Yu, W. Wang, *Nat. Commun.* **2022**, *13*, 5991.
[19] L.-c. Peng, Y. Zhang, S.-l. Zuo, M. He, J.-w. Cai, S.-g. Wang, H.-x. Wei, J.-q. Li, T.-y. Zhao, B.-g. Shen, *Chin. Phys. B* **2018**, *27*, 066802.
[20] J. Cui, Y. Yao, X. Shen, Y. Wang, R. Yu, *J. Magn. Magn. Mater.* **2018**, *454*, 304.
[21] F. Gómez-Ortiz, P. García-Fernández, J. M. López, J. Junquera, *Phys. Rev. B* **2022**, *106*, 134106.
[22] Y. Nahas, S. Prokhorenko, I. Kornev, L. Bellaiche, *Phys. Rev. Lett.* **2017**, *119*, 117601.
[23] C. Xu, Y. Nahas, S. Prokhorenko, H. Xiang, L. Bellaiche, *Phys. Rev. B* **2020**, *101*, 241402.
[24] S. Chae, N. Lee, Y. Horibe, M. Tanimura, S. Mori, B. Gao, S. Carr, S.-W. Cheong, *Phys. Rev. Lett.* **2012**, *108*, 167603.
[25] J. Kim, M. You, K.-E. Kim, K. Chu, C.-H. Yang, *npj Quantum Mater.* **2019**, *4*, 29.
[26] B. Huang, G. Kong, E. N. Esfahani, S. Chen, Q. Li, J. Yu, N. Xu, Y. Zhang, S. Xie, H. Wen, *npj Quantum Mater.* **2018**, *3*, 30.
[27] W. Ming, B. Huang, J. Li, *J. Mech. Phys. Solids* **2022**, *159*, 104758.
[28] S. Jesse, A. P. Baddorf, S. V. Kalinin, *Nanotechnology* **2006**, *17*, 1615.
[29] E. A. Eliseev, S. V. Kalinin, S. Jesse, S. L. Bravina, A. N. Morozovska, *J. Appl. Phys.* **2007**, *102*, 014109.
[30] C.-L. Jia, V. Nagarajan, J.-Q. He, L. Houben, T. Zhao, R. Ramesh, K. Urban, R. Waser, *Nat. Mater.* **2007**, *6*, 64.
[31] C. T. Nelson, P. Gao, J. R. Jokisaari, C. Heikes, C. Adamo, A. Melville, S.-H. Baek, C. M. Folkman, B. Winchester, Y. Gu, *Science* **2011**, *334*, 968.
[32] P. Gao, H.-J. Liu, Y.-L. Huang, Y.-H. Chu, R. Ishikawa, B. Feng, Y. Jiang, N. Shibata, E.-G. Wang, Y. Ikuhara, *Nat. Commun.* **2016**, *7*, 11318.
[33] Y. Sun, A. Y. Abid, C. Tan, C. Ren, M. Li, N. Li, P. Chen, Y. Li, J. Zhang, X. Zhong, *Sci. Adv.* **2019**, *5*, eaav4355.
[34] C.-L. Jia, K. W. Urban, M. Alexe, D. Hesse, I. Vrejoiu, *Science* **2011**, *331*, 1420.
[35] Y. Tang, Y. Zhu, X. Ma, A. Y. Borisevich, A. N. Morozovska, E. A. Eliseev, W. Wang, Y. Wang, Y. Xu, Z. Zhang, *Science* **2015**, *348*, 547.
[36] Y. Liu, Y.-J. Wang, Y.-L. Zhu, C.-H. Lei, Y.-L. Tang, S. Li, S.-R. Zhang, J. Li, X.-L. Ma, *Nano Lett.* **2017**, *17*, 7258.
[37] A. Yadav, C. Nelson, S. Hsu, Z. Hong, J. Clarkson, C. Schlepütz, A. Damodaran, P. Shafer, E. Arenholz, L. Dedon, *Nature* **2016**, *530*, 198.
[38] M. Guo, C. Guo, J. Han, S. Chen, S. He, T. Tang, Q. Li, J. Strzalka, J. Ma, D. Yi, *Science* **2021**, *371*, 1050.
[39] S. Das, Y. L. Tang, Z. Hong, M. A. P. Goncalves, M. R. McCarter, C. Klewe, K. X. Nguyen, F. Gomez-Ortiz, P. Shafer, E. Arenholz, V. A. Stoica, S. L. Hsu, B. Wang, C. Ophus, J. F. Liu, C. T. Nelson, S. Saremi, B. Prasad, A. B. Mei, D. G. Schlom, J. Iniguez, P. Garcia-Fernandez, D. A. Muller, L. Q. Chen, J. Junquera, L. W. Martin, R. Ramesh, *Nature* **2019**, *568*, 368.
[40] R. Zhu, Z. Jiang, X. Zhang, X. Zhong, C. Tan, M. Liu, Y. Sun, X. Li, R. Qi, K. Qu, *Phys. Rev. Lett.* **2022**, *129*, 107601.
[41] S. Das, Z. Hong, V. A. Stoica, M. A. P. Goncalves, Y. T. Shao, E. Parsonnet, E. J. Marksz, S. Saremi, M. R. McCarter, A. Reynoso, C. J. Long, A. M. Hagerstrom, D. Meyers, V. Ravi, B. Prasad, H. Zhou, Z. Zhang, H. Wen, F. Gomez-Ortiz, P. Garcia-Fernandez, J. Bokor, J. Iniguez, J. W. Freeland, N. D. Orloff, J. Junquera, L. Q. Chen, S. Salahuddin, D. A. Muller, L. W. Martin, R. Ramesh, *Nat. Mater.* **2021**, *20*, 194.
[42] X. Li, C. Tan, C. Liu, P. Gao, Y. Sun, P. Chen, M. Li, L. Liao, R. Zhu, J. Wang, Y. Zhao, L. Wang, Z. Xu, K. Liu, X. Zhong, J. Wang, X. Bai, *Proc. Natl. Acad. Sci. U. S. A* **2020**, *117*, 18954.
[43] C. Dai, V. A. Stoica, S. Das, Z. Hong, L. W. Martin, R. Ramesh, J. W. Freeland, H. Wen, V. Gopalan, L. Q. Chen, *Adv. Mater.* **2022**, *34*, 2106401.

[44] A. R. Damodaran, J. Clarkson, Z. Hong, H. Liu, A. K. Yadav, C. T. Nelson, S.-L. Hsu, M. McCarter, K.-D. Park, V. Kravtsov, *Nat. Mater.* **2017**, *16*, 1003.
[45] P. Chen, C. Tan, Z. Jiang, P. Gao, Y. Sun, L. Wang, X. Li, R. Zhu, L. Liao, X. Hou, *Sci. China: Phys., Mech. Astron.* **2022**, *65*, 237011.
[46] P. Chen, X. Zhong, J. A. Zorn, M. Li, Y. Sun, A. Y. Abid, C. Ren, Y. Li, X. Li, X. Ma, J. Wang, K. Liu, Z. Xu, C. Tan, L. Chen, P. Gao, X. Bai, *Nat. Commun.* **2020**, *11*, 1840.
[47] K. Du, M. Zhang, C. Dai, Z. N. Zhou, Y. W. Xie, Z. H. Ren, H. Tian, L. Q. Chen, G. Van Tendeloo, Z. Zhang, *Nat. Commun.* **2019**, *10*, 4864.
[48] P. Behera, M. A. May, F. Gómez-Ortiz, S. Susarla, S. Das, C. T. Nelson, L. Caretta, S.-L. Hsu, M. R. McCarter, B. H. Savitzky, *Sci. Adv.* **2022**, *8*, eabj8030.
[49] P. Aguado-Puente, J. Junquera, *Phys. Rev. B* **2012**, *85*, 184105.
[50] A. Y. Abid, Y. Sun, X. Hou, C. Tan, X. Zhong, R. Zhu, H. Chen, K. Qu, Y. Li, M. Wu, J. Zhang, J. Wang, K. Liu, X. Bai, D. Yu, X. Ouyang, J. Wang, J. Li, P. Gao, *Nat. Commun.* **2021**, *12*, 2054.
[51] Y. Chen, Y. Tang, Y. Zhu, Y. Wang, M. Han, M. Zou, Y. Feng, W. Geng, F. Gong, X. Ma, *Appl. Phys. Lett.* **2020**, *117*, 192901.
[52] S. Estandía, F. Sánchez, M. F. Chisholm, J. Gázquez, *Nanoscale* **2019**, *11*, 21275.
[53] L. Zhou, C. Dai, P. Meisenheimer, S. Das, Y. Wu, F. Gómez-Ortiz, P. García-Fernández, Y. Huang, J. Junquera, L. Q. Chen, *Adv. Funct. Mater.* **2022**, *32*, 2111392.
[54] D. de Ligny, P. Richet, *Phys. Rev. B* **1996**, *53*, 3013.
[55] J. Chen, X. Xing, R. Yu, G. Liu, *J. Am. Ceram. Soc.* **2005**, *88*, 1356.
[56] T. Yang, C. Dai, Q. Li, H. Wen, L.-Q. Chen, *Phys. Rev. B* **2021**, *103*, L220303.
[57] E. Sardella, P. N. Lisboa Filho, C. C. de Souza Silva, L. R. E. Cabral, W. A. Ortiz, *Phys. Rev. B* **2009**, *80*, 012506.
[58] V. S. Stolyarov, I. S. Veshchunov, S. Y. Grebenchuk, D. S. Baranov, I. A. Golovchanskiy, A. G. Shishkin, N. Zhou, Z. Shi, X. Xu, S. Pyon, *Sci. Adv.* **2018**, *4*, eaat1061.
[59] S. Kim, C.-R. Hu, M. J. Andrews, *Phys. Rev. B* **2006**, *74*, 214511.
[60] L. F. Chibotaru, A. Ceulemans, V. Bruyndoncx, V. V. Moshchalkov, *Nature* **2000**, *408*, 833.
[61] M. Iavarone, A. Scarfato, F. Bobba, M. Longobardi, G. Karapetrov, V. Novosad, V. Yefremenko, F. Giubileo, A. Cucolo, *Phys. Rev. B* **2011**, *84*, 024506.
[62] D. Kim, A. Goldman, J. Kang, R. Kampwirth, *Phys. Rev. B* **1989**, *40*, 8834.
[63] C. Tan, Y. Dong, Y. Sun, C. Liu, P. Chen, X. Zhong, R. Zhu, M. Liu, J. Zhang, J. Wang, *Nat. Commun.* **2021**, *12*, 4620.
[64] C.-L. Jia, V. Nagarajan, J.-Q. He, L. Houben, T. Zhao, R. Ramesh, K. Urban, R. Waser, *Nat. Mater.* **2007**, *6*, 64.
[65] W. Zhong, R. King-Smith, D. Vanderbilt, *Phys. Rev. Lett.* **1994**, *72*, 3618.
[66] Y. Su, C. M. Landis, *J. Mech. Phys. Solids* **2007**, *55*, 280.
[67] Z. Li, M. Grimsditch, X. Xu, S.-K. Chan, *Ferroelectrics* **1993**, *141*, 313.
[68] Y. Li, S. Hu, Z. Liu, L. Chen, *Acta Mater.* **2002**, *50*, 395.